Monolayer $C2/m$-SnX (X = P, As): An in-plane anisotropic two-dimensional direct band gap semiconductor with ultrahigh mobility, ideal IR-VIS light transparency, and high absorbance

Qing-Yuan Chen,[1,*] Fei-Jie Huang,[1] Ju-Qi Ruan,[1] Tai Ma,[2] Kai Xiong,[3] and Yao He[4,†]

[1]*School of Physical Science and Technology, Kunming University, Kunming 650214, China*

[2]*Department of Physics, West Yunnan University of Applied Sciences, No. 2, Haiyue Street, Dali 671000, Yunnan Province, China*

[3]*Materials Genome Institute, School of Materials and Energy, Yunnan University, Kunming 650091, China*

[4]*Department of Physics, Yunnan University, No. 2 Green Lake North Road, Wu Hua Qu, Kunming 650091, Yunnan Province, China*

(Received 19 August 2022; revised 12 October 2022; accepted 18 October 2022; published 28 October 2022)

Over the years, designing and establishing new materials with good stability, a suitable band gap, and high carrier mobility have become the focus in researching two-dimensional (2D) materials. In this paper, we predict two 2D semiconductors, $C2/m$-SnX (X = P, As), using first-principles simulation. They possess excellent dynamical and thermal stability, low structural symmetry, high cohesive energy, and good flexibility for the structural properties. Regarding electronic properties, SnP and SnAs are direct band gap semiconductors with suitable band gap values. In addition, they exhibit a high carrier mobility (about $\sim 10^3$–10^4 cm^2 V^{-1} s^{-1}). Their optical properties reveal good transparency in the infrared and visible light regions, but the primary response region of light locates in the ultraviolet area. In addition, their electronic and optical properties show different characteristics in different directions. Therefore, $C2/m$-SnX (X = P, As) are 2D direct band gap semiconductors with excellent stability, a suitable band gap value, high carrier mobility, and good IR-VIS light transparency. We suggest that the group IV-V 2D semiconductor $C2/m$-SnX (X = P, As) will have bright prospects in field-effect transistors, integrated circuits, the hole transport layer of solar cells, blue LEDs, and other nanoelectronic and nano-optoelectronic devices.

DOI: 10.1103/PhysRevMaterials.6.104005

I. INTRODUCTION

The successful preparation of monolayer graphene makes two-dimensional (2D) materials one of the most active research areas in different fields [1–15]. Over the last decade of studies of 2D materials, the family members of 2D materials have been expanding [1–15]. 2D materials exhibit many novel and excellent characteristics compared with bulk materials [1–15]. Different types of 2D materials with outstanding properties have attracted extensive attention in different scientific fields [1–15].

However, current research reveals that 2D materials have many problems yet to be resolved. For example, graphene shows exceptionally high carrier mobility and excellent stability, yet its zero band gap limits its wide applications in various semiconductor fields [16–19]. Another example is that although black phosphorene has a suitable band gap value, high carrier mobility, and prominent anisotropy, its poor stability at high temperature restricts its practical applications [20,21]. Likewise, 2D transitional metal dichalcogenides (TMDs) have good stability and a suitable band gap, but their carrier mobility is low [1,4,5,22–24]. Therefore, the design and preparation of 2D materials with excellent stability, a suitable band gap, high carrier mobility, and easy exfoliation is one of the most urgent problems in the field of 2D materials.

In recent years, the main approaches to solve this problem contain the following two aspects: designing and preparing novel 2D materials, and modifying and optimizing existing 2D materials. Both aspects have so far achieved much progress. Recently, 2D group IV-V semiconductors have become a new class of 2D materials with great potential in a wide range of nanoelectronic and nano-optoelectronic fields.

In 2016, Ashton *et al.* used first-principles calculations to predict a series of 2D IV-V materials belonging to the *Cm* and space group. They found that IV-V materials can form type II heterojunctions; moreover, a few 2D IV-V materials are stable when exposed to water [25]. Barreteau *et al.* successfully prepared 2D layered $C2/m$-SiAs, GeP, GeAs, and $Cmc2$-SiP semiconductors using the melt-growth method under high pressure [26]. Zhang *et al.* studied monolayer $C2/m$-SiP using first-principles calculations. They found that monolayer $C2/m$-SiP is a dynamic and thermal stable semiconductor with a wide direct band gap (2.59 eV) and suggested that it has good application prospects in the field of blue LEDs [27].

In 2017, Li *et al.* used the seeded flux method to synthesize $Cmc2$-SiP single crystals successfully. They measured that its band gap is 1.71 eV, its carrier mobility could reach 2.034×10^3 cm^2 V^{-1} s^{-1}, and it can maintain good thermal stability at 1045 °C. They believe that 2D $Cmc2$-SiP can be a promising candidate in electricity and photoelectric fields [28].

In 2018, Cheng *et al.* found that single-layer SiP, SiAs, GeP, and GeAs are wide band gap semiconductors with good dynamic and thermal stability, and all exhibit a transition between a direct and indirect band gap under strain [29]. Jung *et al.* studied 2D GeAs via experiments and density functional theory (DFT) calculations. They found that multilayer GeAs is a promising photoelectric material with good responsivity in

*Corresponding author: qingyuanchen212@163.com

†Corresponding author: yhe@ynu.edu.cn

the visible light region [30]. Li *et al.* explored 2D GeP through experiments and first-principles calculations and found that it is a 2D semiconductor with high conductance and photoresponsive anisotropy [31].

In 2019, Guo *et al.* found that 2D Ge-P compounds have a good application potential as new nonlinear optics (NLO) materials in the field of ultrafast photons [32]. Jiao *et al.* found that monolayer Ge-P compounds are promising materials for sunlight-driven water splitting [33].

In 2020, Yang *et al.* prepared ultrathin GeP nanosheets using the lithiation-assisted chemical exfoliation method and found that 2D GeP shows good sodium storage performance [34].

In 2021, Abboud *et al.* studied the phase transition of GeN between $C2/m$ and $P\bar{3}m1$ under strain. Zeng *et al.* used DFT calculations to investigate the anisotropic carrier mobility of XAs (X = Si or Ge) [35]. Sar identified 2D SiP as an excellent candidate for nonlinear optical materials [36].

In 2022, Abboud *et al.* studied the structural, electric, and optical properties of $C2/m$-GeX (X = N, P, As, Sb, and Bi) monolayers using the first-principles method and found that $C2/m$-GeX has a good application prospect in high-performance flexible nanoelectronic applications [37]. The same year, Ren studied 2D GeP with high photothermal conversion efficiency as a degradable nanosheet for multimodal cancer theranostics [38].

Inspired by these studies, we desire to predict a 2D group IV-V semiconductor with excellent stability, a suitable band gap, high carrier mobility, and improved optical properties to expand the family members of the 2D group IV-V family and further propel its application as a high-performance 2D material in the nanoelectronic and nano-optoelectronic fields.

This paper uses first-principles calculations to predict two 2D group IV-V semiconductors, $C2/m$-SnX (X = P, As). Regarding structural properties, monolayer $C2/m$-SnX (X = P, As) with low structural symmetry and high cohesive energy possesses excellent dynamical and thermal stability. As for the electronic properties, monolayer $C2/m$-SnP and SnAs are direct band gap semiconductors, and their band gap values are 2.103 and 1.698 eV using the Heyd-Scuseria-Ernzerhof screened hybrid functional (HSE06) method. The carrier mobility reaches up to $\sim 10^3$–10^4 cm^2 V^{-1} s^{-1}. In terms of the optical properties, the primary light response region locates in the ultraviolet area, whereas they reveal good transparency in the infrared and visible light regions. In addition, their electronic and optical properties show different characteristics in different directions. Based on our results, $C2/m$-SnX (X = P, As) are 2D direct band gap semiconductors with excellent stability, good flexibility, a suitable band gap value, high carrier mobility, and good transparency in IR-VIS light. Furthermore, we suggest that they could be a promising candidate in field-effect transistors, integrated circuits, the hole transport layer of solar cells, blue LEDs, and other nanoelectronic and nano-optoelectronic fields.

II. COMPUTATIONAL METHOD

The Vienna *ab initio* simulation package (VASP), created, distributed, and maintained by the Hafner Research Group at the University of Vienna, is adopted for all of our first-principles calculations in this work [39,40]. During the calculations, the projector augmented-wave (PAW) approximation method processed the interaction between electrons [40,41]. The cutoff energy of the plane wave was 600 eV. The exchange-correlation energy was managed by the generalized gradient approximate method established by Perdew, Burke, and Ernzerhof (GGA-PBE) [39,42]. The energy accuracy of convergence was 10^{-6} eV in our structure relaxation calculations. To eliminate the interaction between different layers, we added a vacuum with 30 Å in the **z** direction for the monolayer $C2/m$-SnX structure model. In addition, considering $C2/m$-SnX (X = P, As) contains Sn-d and As-d electrons, we did a comparative calculation with and without spin-orbit coupling (SOC) in the band structure calculations. Furthermore, we employed the HSE06 hybrid functional method to improve the accuracy of the electronic and optical properties results [43,44].

III. RESULTS

A. Structural properties

After sufficient structural relaxation, we obtained the optimized crystal structure of 2D $C2/m$-SnX (X = P, As) (Fig. 1). The framework surrounded by the dotted line is the unit cell. A unit cell contains 12 Sn atoms and 12 X atoms. The lattice parameters of SnP are $a = 3.936$ Å, $b = 23.500$ Å, $\alpha = 92.299^\circ$, $\beta = 90.000^\circ$, and $\gamma = 90.000^\circ$. The Sn-Sn bond lengths are 2.875 and 2.878 Å, and the Sn-P bond lengths are 2.675, 2.683, 2.662, 2.698, 2.677, and 2.670 Å, respectively. In addition, the lattice parameters of SnAs are $a = 4.077$ Å, $b = 24.159$ Å, $\alpha = 91.746^\circ$, $\beta = 90.000^\circ$, and $\gamma = 90.000$Å. The Sn-Sn bond lengths are 2.878 and 2.875 Å, and the Sn-As bond lengths are 2.698, 2.677, 2.662, 2.683, 2.675, and 2.670 Å, respectively. The thicknesses of monolayer SnP and SnAs are 5.820 and 5.924 Å.

In order to verify the structural stability of $C2/m$-SnX (X = P, As), we calculated their phonon spectrum and used the *ab initio* molecular dynamics simulation (AIMD) (Figs. 2 and 3). Figure 2 shows no imaginary frequency of SnP and SnAs in the whole Brillouin zone, which indicates that the established $C2/m$-SnX structure is dynamically stable. Figure 3 exhibits the structural snapshots of monolayer SnX at 0 and 5 ps when applying AIMD simulation at 300 K. The deformation of SnX is not obvious. Results suggest the structures could maintain good stability at room temperature and demonstrate that SnX is thermally stable.

Additionally, we calculated the cohesive energy (E_{coh}), which is defined as

$$E_{\mathrm{coh}} = \frac{n_{\mathrm{Sn}} E_{\mathrm{Sn}}^{\mathrm{atom}} + n_X E_X^{\mathrm{atom}} - E_{\mathrm{Sn}X}}{n_{\mathrm{Sn}} + n_X}, \tag{1}$$

where n_{Sn} and n_X denote the number of tin and phosphorus/arsenic atoms in a unit cell. The indices $E_{\mathrm{Sn}}^{\mathrm{atom}}$ and E_X^{atom} are the energies of the Sn atom and X atom, respectively. $E_{\mathrm{Sn}X}$ represents the total energy of monolayer SnX. Our calculations reveal that the cohesive energies of SnP and SnAs are 5.17 and 4.81 eV/atom, respectively. When the same calculation method is applied, the cohesive energies of other 2D materials such as graphene, silene phosphorene, and monolayer SiP are 7.95, 3.71, 3.24, and 4.21 eV/atom,

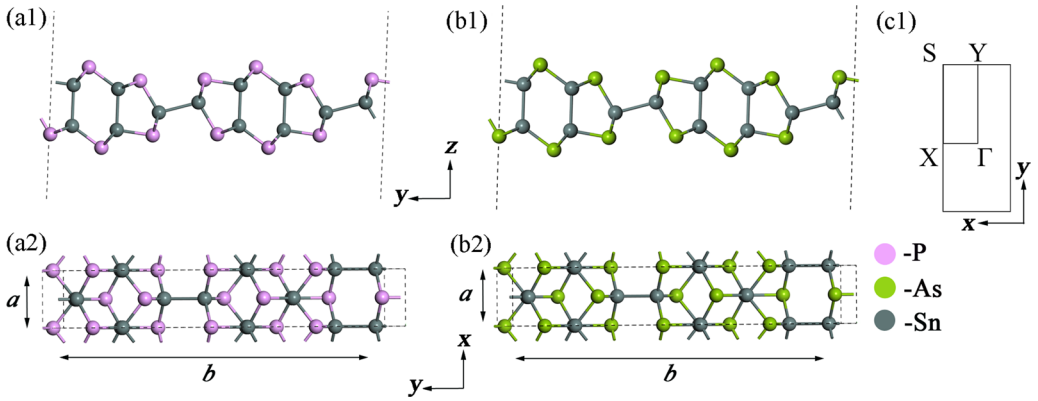

FIG. 1. (a1) and (a2) are the side view and top view of the structure of monolayer $C2/m$-SnP. (b1) and (b2) are the side view and top view of the structure of monolayer $C2/m$-SnAs. (c1) is the Brillouin zone of monolayer $C2/m$-SnX (X = P, As).

respectively [30]. Thus monolayer $C2/m$-SnX is a strongly bonded 2D material with good stability [45].

B. Electronic properties

Next, we discuss the electronic properties of monolayer $C2/m$-SnX (X = P, As). Since Sn and As in SnX (X = P, As) contain d electrons, we first performed comparative calculations on the band structures using GGA-PBE with spin-orbit coupling (SOC) and GGA-PBE without SOC, respectively (Fig. 4). Results show that the band gaps of SnP and SnAs calculated by PBE without the SOC method are 1.416 and 1.104 eV, respectively. However, when considering the SOC effect, the band gaps of SnP and SnAs are 1.409 and 1.051 eV, respectively. In addition, regardless of whether we include the SOC effect, the positions of the valence band maximum (VBM) and conduction band minimum (CBM) of SnX remain unchanged, and it remains a direct band gap semiconductor. Namely, the effect of SOC only slightly diminishes the calculated band gap. Therefore, our subsequent discussions are based on the calculated results without the SOC effect.

Next, we discuss the results with high accuracy obtained by the HSE06 hybrid functional method. First, Fig. 5 shows the calculated band structure of monolayer $C2/m$-SnP and SnAs.

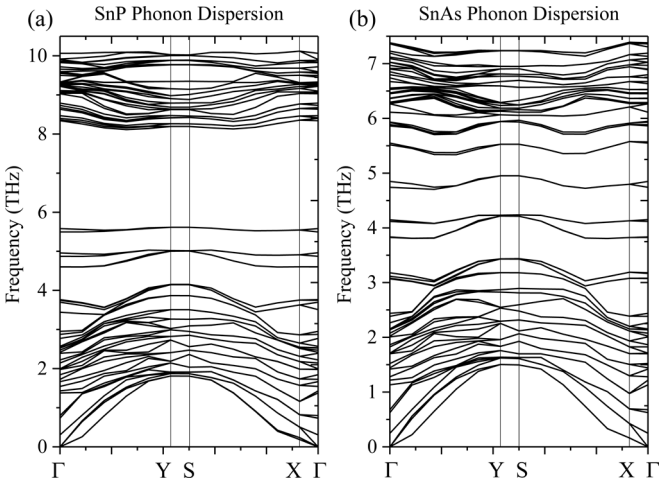

FIG. 2. The phonon dispersion spectrum of (a) SnP and (b) SnAs.

The Fermi level is set to zero. Both SnP and SnAs belong to direct band gap semiconductors, and their band gap values are 2.103 and 1.698 eV, respectively. Compared with GeX and SiX, the band gaps of monolayer $C2/m$-SnP and SnAs are smaller than monolayer GeP (2.309 eV), GeAs (2.077 eV), SiP (2.641 eV), and SiAs (2.353 eV). The suitable size of the direct band gap makes monolayer $C2/m$-SnP and SnAs have great application prospects in the field of semiconductive materials and photoelectric materials.

Furthermore, in order to have a complete understanding of the band structure around the band gap, we calculated the projected band structure and the partial density of states of each element of monolayer SnP and SnAs (Figs. 6 and 7). We can see that the VBM of monolayer SnX is mainly composed of Sn-p and X-p electrons. In comparison, the CBM is mainly composed of Sn-s and X-p electrons and a minimal amount of Sn-p and Sn-d electrons.

Figure 8 exhibits the calculated electron localization function (ELF). We calculated the ELF by using the following definition,

$$\mathrm{ELF} = \frac{1}{1 + \left[\frac{D}{D_h}\right]^2}, \tag{2}$$

where D and D_h are the kinetic energy densities of electron pairs and the uniform electron gas, respectively [46–49].

The value of ELF ranges from 0 to 1. ELF = 0, 0.5, and 1 indicate that the electron is in the complete nonlocality, electron-gas, and perfect localization state, respectively. In addition, if the ELF value near the central position between the bond is beyond 0.75, it demonstrates that the chemical bond forms covalent bonds [37,47,50,51]. Consequently, the Sn-Sn bonds of monolayer SnX should be covalent. However, the electrons between Sn and X exhibit the electron-gas characteristics, indicating that the Sn-X bonds are composed of partial covalent bonds and partial metallic bonds. The existence of the electron-gas characteristics allows monolayer SnX to be flexible [37]. Additionally, the electrons of monolayer SnX mainly concentrate on the outside of the X atom, which indicates there are lone-pair electrons (LPEs) around X. The electrons' transition from Sn to X should be mainly due to the electronegativity difference between Sn and X. Moreover, the LPEs could lead to the high carrier mobility of SnX.

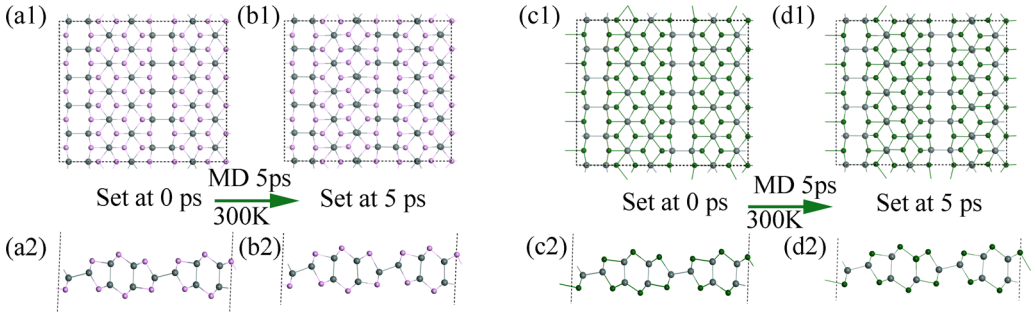

FIG. 3. (a1), (a2), (c1), and (c2) represent the structure of the SnX (X = P, As) supercell before AIMD simulation. (b1), (b2), (d1), and (d2) represent the structure of the monolayer SnX (X = P, As) supercell after applying AIMD simulation at 300 K and 5 ps.

In order to have a more comprehensive understanding of the electronic properties of SnX, we calculated the carrier mobility properties at 300 K based on the deformation potential (DP) theory [52–55]. The main equations involved in the calculation process are defined as

$$\mu_{2D} = \frac{2e\hbar^3 C}{3k_B T|m^\star|^2 E_1^2} \tag{3}$$

$$\tau = \frac{\mu_{2D} m^\star}{e}, \tag{4}$$

$$m^\star = \hbar^2 \left[\frac{\partial^2 E}{\partial k^2}\right]^{-1}, \tag{5}$$

$$C = \left[\frac{\partial^2 E}{\partial(\Delta a/a_0)^2}\right] S_0^{-1}, \tag{6}$$

$$E_1 = \frac{\partial E_{\text{edge}}}{\partial(\Delta a/a_0)}, \tag{7}$$

where μ_{2D}, τ, m^*, C, and E_1 denote the carrier mobility, relaxation time, effective mass, elastic constant, and DP energy, respectively. The index E is the total energy of monolayer SnX under strain, and E_{edge} is the shift of the band edge, including the vacuum energy level. The relaxation time shown in Table I is obtained by converting μ_{2D} to τ using Eq. (3). Δa is the lattice parameter change between the strained and strain-free structure, and a_0 is the lattice constant of strain-free SnX. Since the structural symmetries along the **x** and **y** directions are low, we considered the carrier mobilities along the **x** and **y** directions separately. The calculated results are shown in Table I. We found that the electron and hole mobilities of monolayer SnP along the **x** direction are 1.488×10^3 and 9.79×10^3 cm^2 V^{-1} s^{-1}, and the electron and hole mobilities along the **y** direction are 841.296 and 1.869×10^3 cm^2 V^{-1} s^{-1}. In addition, the electron and hole mobilities of monolayer SnAs along the **x** direction are 1.882×10^3 and 2.215×10^4 cm^2 V^{-1} s^{-1}, and the electron and hole mobilities along the **y** direction are 1.537×10^3 and 6.458×10^3 cm^2 V^{-1} s^{-1}, respectively. The hole mobility is always higher than the electron mobility. At room temperature, its electron mobility is higher than that of black phosphorene (1000 cm^2 V^{-1} s^{-1}), and its carrier mobility almost reaches a similar order of magnitude as that of graphene. Moreover, the relaxation time of both holes and electrons can achieve 10^2–10^3 fs at room temperature, leading to the high carrier mobility and stable and efficient electrical conductivities.

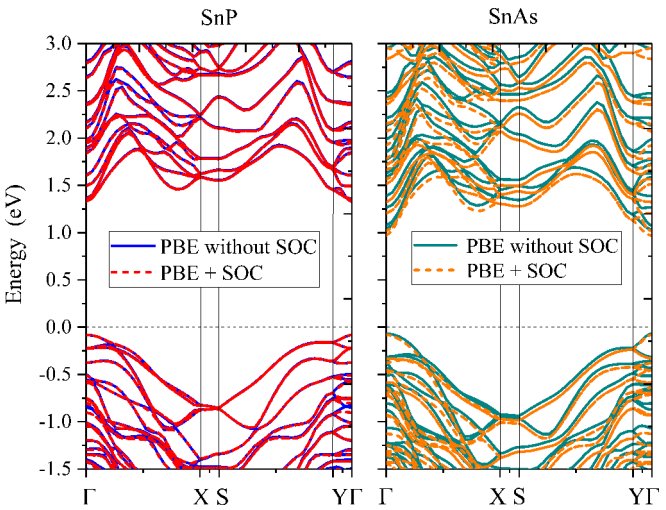

FIG. 4. The calculated band structures of $C2/m$-SnP (left) and SnAs (right) using PBE without the SOC effect and PBE+SOC effect, respectively.

The reasons for the high electron mobility of monolayer SnX are mainly caused by the following factors. One is the existence of the LPEs on the outer side of the X atom, and the electron localization in the layer is weak (see Fig. 8). The other is that monolayer SnX exhibits a tiny effective mass of electrons and a long relaxation time. For instance, the effective mass of electrons for black phosphorene, h-BN, MoS_2, CaP_3, $CaAs_3$, SnP_3, and SnS are 1.12, 0.99, 0.48, 0.80, 2.04, 0.92, and 0.51 eV, respectively, and so on. By comparison, the effective mass of electrons for monolayer SnX is much smaller [56,57]. Similarly, we suggest the reasons for the high hole mobility of monolayer SnX are primarily due to the holes' small effective mass, long relaxation time, and small elastic constant.

Furthermore, the small carrier effective mass and high carrier mobility of SnX could lead to relativistic behavior. This, in turn, produces a linear band structure feature around the VBM and CBM, which is similar to the band structure of graphene [58–61]. Such a band structure feature can be verified in Fig. 9, which exhibits a band structure [Figs. 9(a1) and 9(b1)] and 3D band structure [Figs. 9(a2)–9(a4) and 9(b2)–9(b4)] of VBM and CBM for monolayer SnX using the

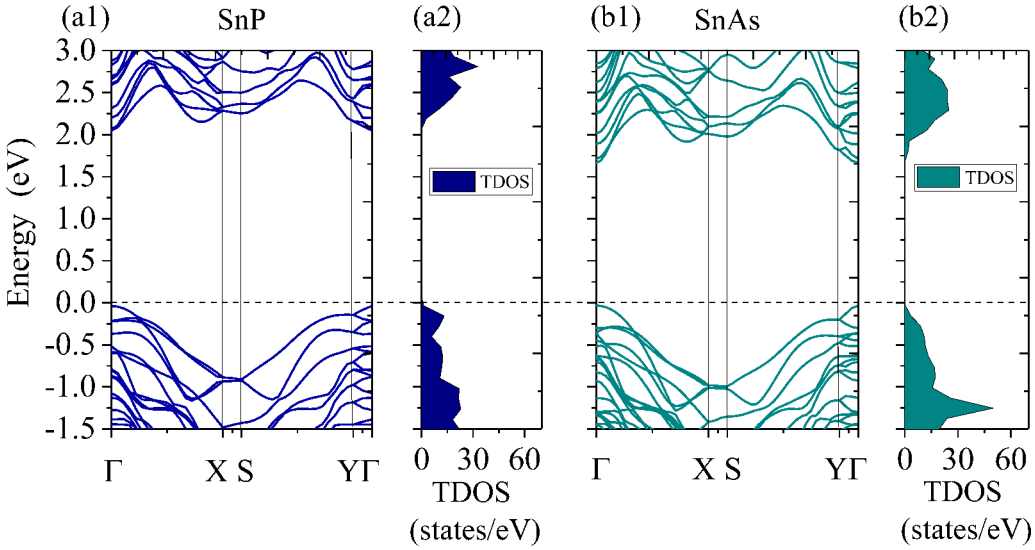

FIG. 5. (a1) and (b1) are the calculated band structures of monolayer $C2/m$-SnP and SnAs using the HSE06 method. (a2) and (b2) are the total density of states of monolayer $C2/m$-SnP and SnAs using the HSE06 method.

HSE06 method. We found that, around the position of CBM and VBM (Γ point), the band structure of SnX reveals a linear shape rather than a parabolic shape.

As a 2D material, monolayer $C2/m$-SnX (X = P, As) has excellent electronic properties such as a suitable direct band gap, high carrier mobility, and long relaxation time. These

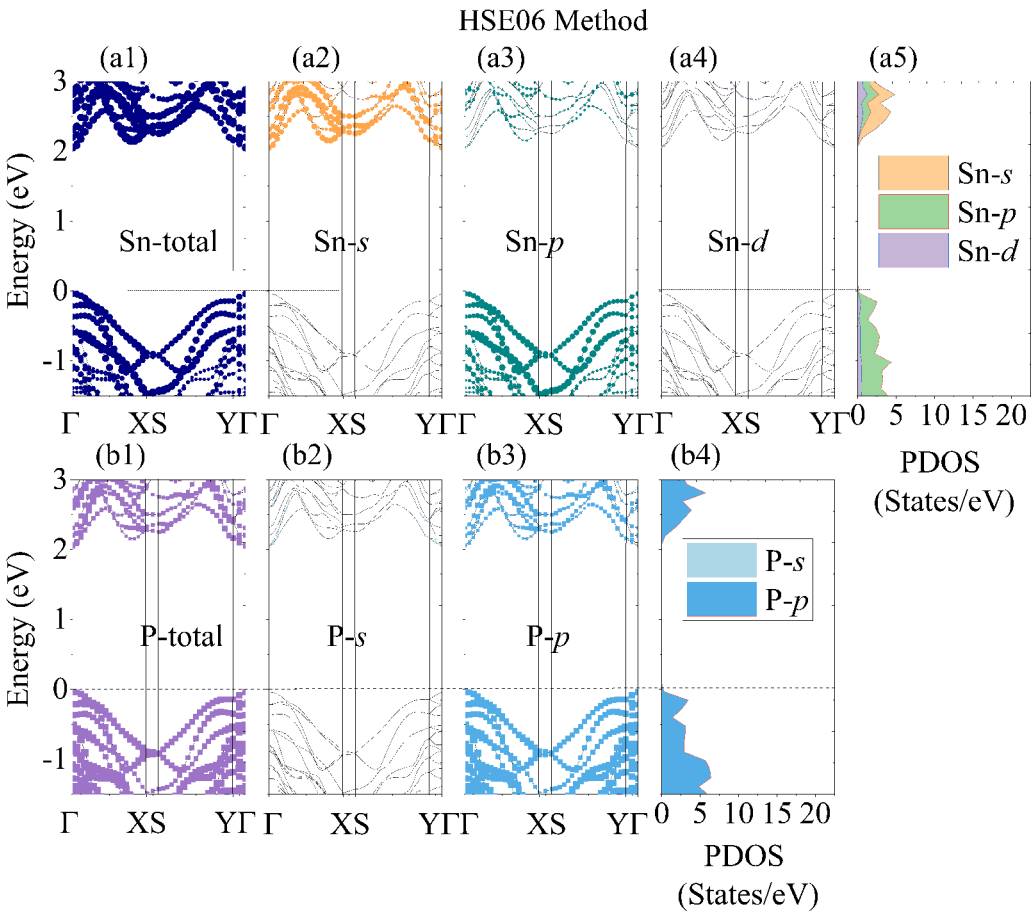

FIG. 6. (a1), (b1) Monolayer SnP projected band structure of the Sn and P method. (a2)–(a4) The projected band structure of Sn-s, Sn-p, and Sn-d electrons, respectively. (b2)–(b4) The projected band structure of P-s, P-p, and P-d electrons, respectively. (a5), (b5) The partial density of states of monolayer SnP using the HSE06 method.

TABLE I. The calculated carrier mobility (μ), relaxation time (τ), effective mass (m^*), elastic constant (E_1), and DP energy (C) of $C2/m$-SnP and SnAs.

Material	Carrier type	m_x^* (m_e)	m_y^* (m_e)	E_{1x} (eV)	E_{1y} (eV)	C_{2D-x} (N/m)	C_{2D-y} (N/m)	μ_x (cm^2 V^{-1} s^{-1})	μ_y (cm^2 V^{-1} s^{-1})	$\tau_x(fs)$	$\tau_y(fs)$
	e	0.212	0.269	4.393	4.615			1.488×10^3	841.296	176.785	126.873
SnP	h	1.239	0.617	0.293	1.350	90.487	90.938	9.79×10^3	1.869×10^3	6.8×10^3	643.208
	e	0.145	0.304	5.318	2.831			1.882×10^3	1.537×10^3	152.976	261.95
SnAs	h	0.966	0.270	0.237	1.555	78.482	79.846	2.135×10^4	6.458×10^3	1.156×10^4	977.567

unique characteristics can make 2D $C2/m$-SnX (X = P, As) have a bright application prospect in the field of semiconductor electronics such as field-effect transistors, integrated circuits, etc.

C. Optical properties

A suitable direct band gap and ultrahigh charge mobility allow us to have full expectations for the optical properties of 2D $C2/m$-SnX (X = P, As). We first calculate the imaginary part of its dielectric function $\varepsilon_2(\omega)$ using Eq. (6). Then we obtained the real part of the dielectric function $\varepsilon_1(\omega)$ by the Kramers-Kronig relation [Eq. (7)] [62]. According to the relationship between the complex dielectric function and the optical absorption coefficient [$I(\omega)$] and reflection coefficient [$R(\omega)$] [Eqs. (8)–(10)], we gained the optical absorption and reflection properties of monolayer SnX. In these equations, the symbols c and v represent the band states of conduction and valence, respectively. The u_{ck} refers to the cell periodic part of the wave functions at the k point. Namely, we identify the principal value as P. As with the electronic properties, we discuss the optical properties obtained by using the HSE06 method (the solid lines in Figs. 9 and 10):

$$\varepsilon_2(\omega) = \frac{4\pi^2 e^2}{\Omega} \lim_{q\to 0} \frac{1}{q^2} \sum_{c,v,k} 2w_k \delta(\varepsilon_{ck} - \varepsilon_{vk} - \omega) \langle u_{ck+e_{\alpha q}} | u_{vk} \rangle \times \langle u_{ck+e_{\beta q}} | u_{vk} \rangle^*, \tag{8}$$

$$\varepsilon_1(\omega) = 1 + \frac{2}{\pi} P \int_0^\infty \frac{\varepsilon^{(2)}_{\alpha\beta}(\omega')\omega'}{\omega'^2 - \omega^2 + i\eta} d\omega', \tag{9}$$

$$\varepsilon(\omega) = \varepsilon_1(\omega) + i\varepsilon_2(\omega), \tag{10}$$

$$I(\omega) = \frac{\sqrt{2}}{c} \omega [\sqrt{\varepsilon_1(\omega)^2 + \varepsilon_2(\omega)^2} - \varepsilon_1(\omega)]^{1/2}, \tag{11}$$

$$R(\omega) = \left| \frac{\sqrt{\varepsilon(\omega)} - 1}{\sqrt{\varepsilon(\omega)} + 1} \right|^2 = \frac{(n-1)^2 + k^2}{(n+1)^2 + k^2}. \tag{12}$$

Figure 10 shows the calculated optical properties of the monolayer SnP. In the **x** direction, the absorption edge is 2.389 eV, and the absorption coefficient can reach 1.68×10^4 cm^{-1} in the visible light region, while the main absorption range is located in the ultraviolet light and deep ultraviolet light region, and the maximum absorption peak appears at

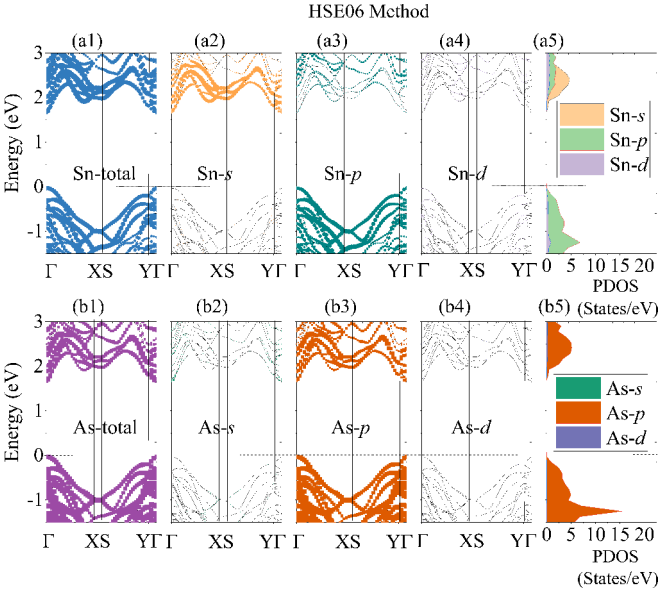

FIG. 7. (a1), (b1) Monolayer SnAs projected band structure of Sn and As method. (a2)–(a4) The projected band structure of Sn-s, Sn-p, and Sn-d electrons, respectively. (b2)–(b4) The projected band structure of As-s, As-p, and As-d electrons, respectively. (a5), (b5) The partial density of states of monolayer SnAs using the HSE06 method.

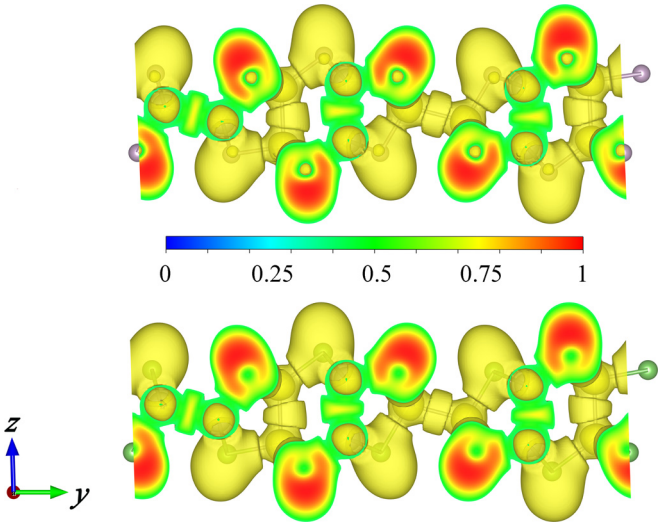

FIG. 8. (a1), (b1) The electron localization function (ELF) spectrum of SnP (top) and SnAs (bottom), where the isosurface value is set to 0.39.

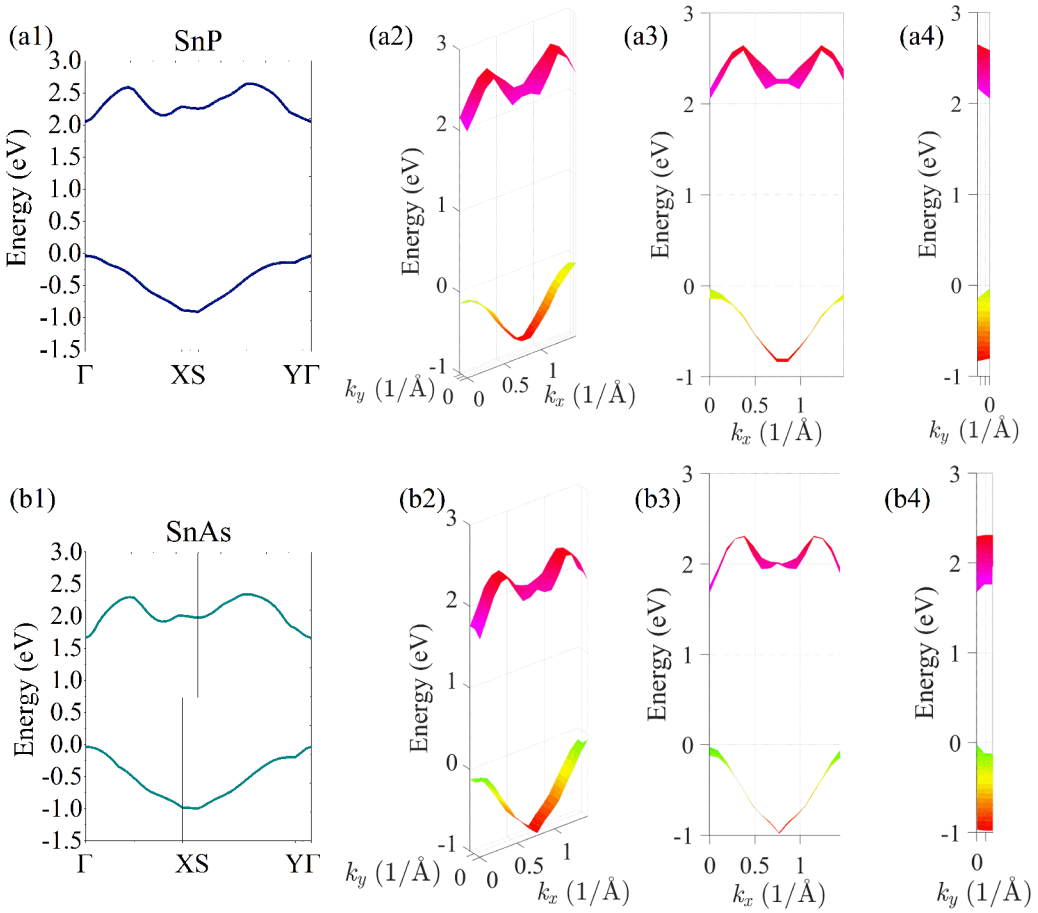

FIG. 9. The band structure (a1) and 3D band structure (a2)–(a4) of VBM and CBM for monolayer SnP using the HSE06 method. The band structure (b1) and 3D band structure (b2)–(b4) of VBM and CBM for monolayer SnAs using the HSE06 method. The band structures of SnX around the positions of CBM and VBM (Γ point) reveal a linear feature, which verifies the relativistic behavior of SnX.

5.7021 eV with a peak value of 12.12×10^4 cm^{-1}. When the photon energy is greater than 17 eV, the absorption coefficient decreases to zero. Its static reflection coefficient is 5.78%, and the reflection coefficient is between 6.9% and 12.8% in the range of visible light. The maximum reflection peak at 5.7977 eV of the peak value is 30.07%. When the photon energy exceeds 15 eV, its reflection coefficient decreases to zero. The **y** direction's absorption edge is 2.0706 eV, and its absorption coefficient can achieve 2.17×10^4 cm^{-1} in the visible region. The primary absorption area lies in the ultraviolet and deep ultraviolet regions, and the maximum absorption peak occurs at 5.957 eV with a peak value of 11.16×10^4 cm^{-1}. In the range of the energy beyond 17 eV, its absorption coefficient decreases to zero. The static reflection coefficient is 5.98%, and its reflection coefficient is between 7.44% and 13.41% in the visible light region. The maximum reflection peak of 26.99% is located at 6.0525 eV. Its reflection coefficient decreases to zero when the energy surpasses 15 eV.

Figure 11 exhibits the optical properties of the monolayer SnAs. Regarding the absorption properties, the absorption edge in the **x** and **y** directions is 1.9854 and 1.733 eV, respectively. The absorption coefficient in the visible light region can reach 2.73×10^4 cm^{-1} (**x** direction) and 3.91×10^4 cm^{-1}. The main absorption range in the **x** and **y** directions is located in the ultraviolet light and deep ultraviolet light region. Its maximum absorption peak in the **x** and **y** direction appears at 5.3258 eV with a peak value of 10.98×10^4 cm^{-1} and 5.3889 eV with a peak value of 11.09×10^4 cm^{-1}, respectively. When the photon energy is greater than 17 eV, the absorption coefficients decrease to zero. In terms of the reflection properties, the static reflection coefficient is 6.96% and 7.09% in the **x** and **y** directions. The reflection coefficient in the visible light region is 8.89%–15.42% in the **x** direction and 9.88%–16.64% in the **y** direction. The maximum reflection peak at 5.641 eV of the peak value is 28.76% (**x** direction), and 5.7985 eV with the peak value of 30.57% (**y** direction). When the photon energy exceeds 15 eV, its reflection coefficient decreases to zero.

Combining the absorption and reflection properties, we find that monolayer $C2/m$-SnX (X = P, As) possesses excellent transparency in the infrared light or even the visible light region. In addition, it shows different optical properties in the **x** and **y** directions.

In short, monolayer $C2/m$-SnX (X = P, As) shows good transparency in the IR-VIS light regions. The major light response region lies in the ultraviolet area. Also, the high charge mobility generally leads to the material exhibiting ideal optical properties [57]. Combined, 2D SnX should have

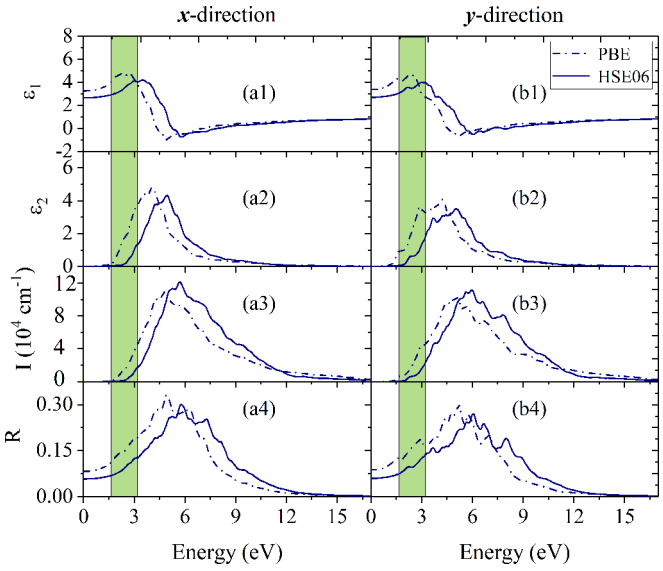

FIG. 10. The optical properties of monolayer SnP in the **x** and **y** directions using the PBE method (dotted line) and HSE06 method (solid line). $\varepsilon_2(\omega)$, $\varepsilon_1(\omega)$, $I(\omega)$, and $R(\omega)$ denote the imaginary part of the dielectric function, the real part of the dielectric function, absorption coefficient, and reflection coefficient. The green area is the visible light region.

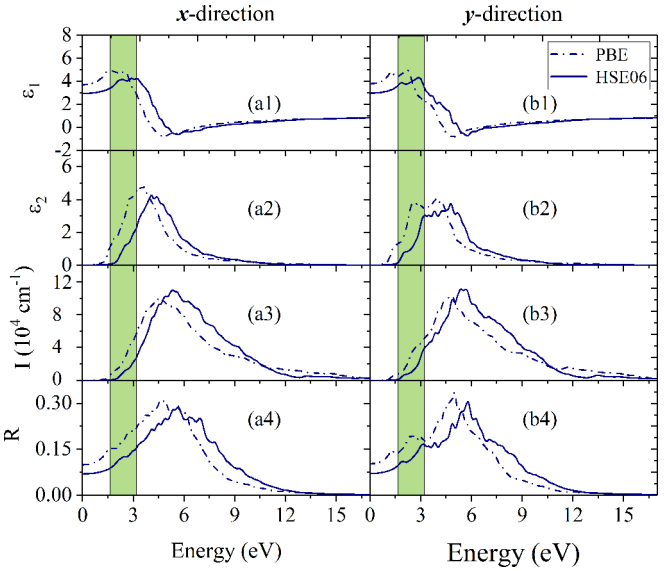

FIG. 11. The optical properties of monolayer SnAs in the **x** and **y** directions using the PBE method (dotted line) and HSE06 method (solid line). $\varepsilon_2(\omega)$, $\varepsilon_1(\omega)$, $I(\omega)$, and $R(\omega)$ denote the imaginary part of the dielectric function, the real part of the dielectric function, absorption coefficient, and reflection coefficient. The green area is the visible light region.

a superior performance in nano-optoelectronic devices, such as the hole transport layer of solar cells, photocatalysts, and blue/UV light-emitting diodes.

IV. CONCLUSIONS

In summary, using first-principles calculations, we predicted two 2D semiconductors, monolayer $C2/m$-SnX (X = P, As), with excellent structural, electronic, and optical properties. We find that monolayer $C2/m$-SnX (X = P, As) is a strongly bonded 2D material with excellent dynamical stability, thermal stability, and flexibility. It has a suitable direct band gap and ultrahigh carrier mobility, and the hole mobility is higher than the electron mobility. These features make 2D SnX a promising candidate in the flexible nanoelectronic field, such as field-effect transistors and integrated circuits. In addition, the optical properties exhibit good transparency in the IR-VIS light regions, but the primary response region of light locates in the ultraviolet area. Moreover, it shows different electronic and optical properties in different directions. Such optical properties render SnX an ideal semiconductor for the field of flexible nano-optoelectronics. For example, it can be the hole transport layer of solar cells, photocatalysts, and light-emitting diodes. Therefore, we suggest that 2D $C2/m$-SnX (X = P, As) should have a bright application prospect in high-performance nanoelectronic and nanophotoelectronic devices.

ACKNOWLEDGMENTS

This research was funded by the National Natural Science Foundation of China (Grant No. 12164050), the Major Science and Technology Project of Precious Metal Materials Genetic Engineering in Yunnan Province (Grants No. 2019ZE001-1, No. 202002AB080001-6, and No. 2018IC058), and the Program for Yunling Scholars in Yunnan Province, Program for Donglu Scholars in Yunnan University, Scientific Research Fund Project of Yunnan Provincial Education Department (No. 2022J0628), Yunnan Fundamental Research Projects (Grants No. 202201AU070019 and No.202201AU070036), and Introduction of Talents Projects (No. XJ20210018).

[1] X. Huang, Z. Zeng, and H. Zhang, Metal dichalcogenide nanosheets: Preparation, properties and applications, Chem. Soc. Rev. **42**, 1934 (2013).

[2] G. R. Bhimanapati, Z. Lin, V. Meunier, Y. Jung, J. Cha, S. Das, D. Xiao, Y. Son, M. S. Strano, V. R. Cooper, L. Liang, S. G. Louie, E. Ringe, W. Zhou, S. S. Kim, R. R. Naik, B. G. Sumpter, H. Terrones, F. Xia, Y. Wang *et al.*, Recent advances in two-dimensional materials beyond graphene, ACS Nano **9**, 11509 (2015).

[3] T. Jiang, K. Yin, C. Wang, J. You, H. Ouyang, R. Miao, C. Zhang, K. Wei, H. Li, H. Chen, R. Zhang, X. Zheng, Z. Xu, X. Cheng, and H. Zhang, Ultrafast fiber lasers mode-locked by two-dimensional materials: Review and prospect, Photonics Res. **8**, 78 (2019).

[4] J. Chen, Q. Huang, H. Huang, L. Mao, M. Liu, X. Zhang, and Y. Wei, Recent progress and advances in the environmental applications of MXene related materials, Nanoscale **12**, 3574 (2020).

[5] H. H. Huang, X. Fan, D. J. Singh, and W. T. Zheng, Recent progress of TMD nanomaterials: Phase transitions and applications, Nanoscale **12**, 1247 (2020).

[6] S. Kang, D. Lee, J. Kim, A. Capasso, H. S. Kang, J.-W. Park, C.-H. Lee, and G.-H. Lee, 2D semiconducting materials for electronic and optoelectronic applications: Potential and challenge, 2D Mater. **7**, 022003 (2020).

[7] J. Ke, F. He, H. Wu, S. Lyu, J. Liu, B. Yang, Z. Li, Q. Zhang, J. Chen, L. Lei, Y. Hou, and K. Ostrikov, Nanocarbon-enhanced 2D photoelectrodes: A new paradigm in photoelectrochemical water splitting, Nano-Micro Lett. **13**, 24 (2020).

[8] K. Khan, A. K. Tareen, M. Aslam, R. Wang, Y. Zhang, A. Mahmood, Z. Ouyang, H. Zhang, and Z. Guo, Recent developments in emerging two-dimensional materials and their applications, J. Mater. Chem. C **8**, 387 (2020).

[9] W. Liu, M. Liu, X. Liu, X. Wang, H. Deng, M. Lei, Z. Wei, and Z. Wei, Recent advances of 2D materials in nonlinear photonics and fiber lasers, Adv. Opt. Mater. **8**, 1901631 (2020).

[10] D. Tyagi, H. Wang, W. Huang, L. Hu, Y. Tang, Z. Guo, Z. Ouyang, and H. Zhang, Recent advances in two-dimensional-material-based sensing technology toward health and environmental monitoring applications, Nanoscale **12**, 3535 (2020).

[11] J. Yao and G. Yang, 2D material broadband photodetectors, Nanoscale **12**, 454 (2020).

[12] G. Chakraborty, I. H. Park, R. Medishetty, and J. J. Vittal, Two-dimensional metal-organic framework materials: Synthesis, structures, properties and applications, Chem. Rev. **121**, 3751 (2021).

[13] Y. Liu, X. Duan, H. J. Shin, S. Park, Y. Huang, and X. Duan, Promises and prospects of two-dimensional transistors, Nature (London) **591**, 43 (2021).

[14] Q. Qiu and Z. Huang, Photodetectors of 2D materials from ultraviolet to terahertz waves, Adv. Mater. **33**, 2008126 (2021).

[15] S. Das, D. Pandey, J. Thomas, and T. Roy, The role of graphene and other 2D materials in solar photovoltaics, Adv. Mater. **31**, 1802722 (2019).

[16] A. Gupta, T. Sakthivel, and S. Seal, Recent development in 2D materials beyond graphene, Prog. Mater. Sci. **73**, 44 (2015).

[17] M. Ye, D. Zhang, and Y. Yap, Recent advances in electronic and optoelectronic devices based on two-dimensional transition metal dichalcogenides, Electronics **6**, 43 (2017).

[18] M. Khazaei, A. Ranjbar, M. Arai, T. Sasaki, and S. Yunoki, Electronic properties and applications of MXenes: A theoretical review, J. Mater. Chem. C **5**, 2488 (2017).

[19] C. Tan, X. Cao, X. J. Wu, Q. He, J. Yang, X. Zhang, J. Chen, W. Zhao, S. Han, G. H. Nam, M. Sindoro, and H. Zhang, Recent advances in ultrathin two-dimensional nanomaterials, Chem. Rev. **117**, 6225 (2017).

[20] S. Bertolazzi, D. Krasnozhon, and A. Kis, Nonvolatile memory cells based on MoS_2/graphene heterostructures, ACS Nano **7**, 3246 (2013).

[21] E. Zhang, W. Wang, C. Zhang, Y. Jin, G. Zhu, Q. Sun, D. W. Zhang, P. Zhou, and F. Xiu, Tunable charge-trap memory based on few-layer MoS_2, ACS Nano **9**, 612 (2015).

[22] C. Tan and H. Zhang, Two-dimensional transition metal dichalcogenide nanosheet-based composites, Chem. Soc. Rev. **44**, 2713 (2015).

[23] M. Chhowalla, H. S. Shin, G. Eda, L. J. Li, K. P. Loh, and H. Zhang, The chemistry of two-dimensional layered transition metal dichalcogenide nanosheets, Nat. Chem. **5**, 263 (2013).

[24] R. Lv, J. A. Robinson, R. E. Schaak, D. Sun, Y. Sun, T. E. Mallouk, and M. Terrones, Transition metal dichalcogenides and beyond: Synthesis, properties, and applications of single- and few-layer nanosheets, Acc. Chem. Res. **48**, 56 (2015).

[25] M. Ashton, S. B. Sinnott, and R. G. Hennig, Computational discovery and characterization of polymorphic two-dimensional IV-V materials, Appl. Phys. Lett. **109**, 192103 (2016).

[26] C. Barreteau, B. Michon, C. Besnard, and E. Giannini, High-pressure melt growth and transport properties of SiP, SiAs, GeP, and GeAs 2D layered semiconductors, J. Cryst. Growth **443**, 75 (2016).

[27] S. Zhang, S. Guo, Y. Huang, Z. Zhu, B. Cai, M. Xie, W. Zhou, and H. Zeng, Two-dimensional sip: an unexplored direct band-gap semiconductor, 2D Mater. **4**, 015030 (2016).

[28] C. Li, S. Wang, X. Zhang, N. Jia, T. Yu, M. Zhu, D. Liu, and X. Tao, Controllable seeded flux growth and optoelectronic properties of bulk o-SiP crystals, CrystEngComm **19**, 6986 (2017).

[29] A. Q. Cheng, Z. He, J. Zhao, H. Zeng, and R. S. Chen, Monolayered silicon and germanium monopnictide semiconductors: Excellent stability, high absorbance, and strain engineering of electronic properties, ACS Appl. Mater. Interfaces **10**, 5133 (2018).

[30] C. S. Jung, D. Kim, S. Cha, Y. Myung, F. Shojaei, H. G. Abbas, J. A. Lee, E. H. Cha, J. Park, and H. S. Kang, Two-dimensional GeAs with a visible range band gap, J. Mater. Chem. A **6**, 9089 (2018).

[31] L. Li, W. Wang, P. Gong, X. Zhu, B. Deng, X. Shi, G. Gao, H. Li, and T. Zhai, 2D GeP: An unexploited low-symmetry semiconductor with strong in-plane anisotropy, Adv. Mater. **30**, 1706771 (2018).

[32] J. Guo, D. Huang, Y. Zhang, H. Yao, Y. Wang, F. Zhang, R. Wang, Y. Ge, Y. Song, Z. Guo, F. Yang, J. Liu, C. Xing, T. Zhai, D. Fan, and H. Zhang, 2D GeP as a novel broadband nonlinear optical material for ultrafast photonics, Laser Photonics Rev. **13**, 1900123 (2019).

[33] N. Jiao, P. Zhou, C. He, J. He, X. Liu, and L. Sun, Low-energy GeP monolayers with natural type-II homojunctions for sunlight-driven water splitting, Phys. Status Solidi RRL **13**, 1900470 (2019).

[34] F. Yang, J. Hong, J. Hao, S. Zhang, G. Liang, J. Long, Y. Liu, N. Liu, W. K. Pang, J. Chen, and Z. Guo, Ultrathin few-layer GeP nanosheets via lithiation-assisted chemical exfoliation and their application in sodium storage, Adv. Energy Mater. **10**, 1903826 (2020).

[35] M. Abboud, D. H. Ozbey, and E. Durgun, Strain-induced structural phase transition in GeN monolayer, Appl. Surf. Sci. **567**, 150793 (2021).

[36] H. Sar, J. Gao, and X. Yang, 2D layered SiP as anisotropic nonlinear optical material, Sci. Rep. **11**, 6372 (2021).

[37] M. Abboud, D. H. Ozbey, M. E. Kilic, and E. Durgun, Investigation of anisotropic mechanical, electronic, and charge carrier transport properties of germanium-pnictogen monolayers, J. Phys. D **55**, 185302 (2022).

[38] X. Ren, W. Liu, H. Zhou, J. Wei, C. Mu, Y. Wan, X. Yang, A. Nie, Z. Liu, X. Yang, and Z. Luo, Biodegradable 2D GeP nanosheets with high photothermal conversion efficiency for multimodal cancer theranostics, Chem. Eng. J. **431**, 134176 (2022).

[39] G. Kresse and J. Furthmuller, Efficient iterative schemes for *ab initio* total-energy calculations using a plane-wave basis set, Phys. Rev. B **54**, 11169 (1996).

[40] G. Kresse and D. Joubert, From ultrasoft pseudopotentials to the projector augmented-wave method, Phys. Rev. B **59**, 1758 (1999).

[41] P. E. Blochl, Projector augmented-wave method, Phys. Rev. B **50**, 17953 (1994).

[42] J. P. Perdew, K. Burke, and M. Ernzerhof, Generalized Gradient Approximation Made Simple, Phys. Rev. Lett. **77**, 3865 (1996).

[43] J. Heyd, G. E. Scuseria, and M. Ernzerhof, Hybrid functionals based on a screened Coulomb potential, J. Chem. Phys. **118**, 8207 (2003).

[44] J. Heyd and G. E. Scuseria, Efficient hybrid density functional calculations in solids: Assessment of the Heyd-Scuseria-Ernzerhof screened Coulomb hybrid functional, J. Chem. Phys. **121**, 1187 (2004).

[45] Y. Li, Y. Liao, and Z. Chen, Be_2C monolayer with quasi-planar hexacoordinate carbons: A global minimum structure, Angew. Chem., Int. Ed. **53**, 7248 (2014).

[46] A. D. Becke and K. E. Edgecombe, A simple measure of electron localization in atomic and molecular-systems, J. Chem. Phys. **92**, 5397 (1990).

[47] B. Silvi and A. Savin, Classification of chemical bonds based on topological analysis of electron localization functions, Nature (London) **371**, 683 (1994).

[48] L. De Santis and R. Resta, Electron localization at metal surfaces, Surf. Sci. **450**, 126 (2000).

[49] Y. Liu, G. Yin, W. An, Y. Ke, and R. Quhe, A computational study of electrical contacts to all-inorganic perovskite $CsPbBr_3$, Nanotechnology **33**, 475701 (2022).

[50] R. J. Clements, J. C. Womack, and C. K. Skylaris, Electron localisation descriptors in ONETEP: A tool for interpreting localisation and bonding in large-scale DFT calculations, Electron. Struct. **2**, 027001 (2020).

[51] A. Savin, O. Jepsen, J. Flad, O. K. Andersen, H. Preuss, and H. G. von Schnering, Electron localization in solid-state structures of the elements: The diamond structure, Angew. Chem., Int. Ed. Engl. **31**, 187 (1992).

[52] J. Bardeen and W. Shockley, Deformation potentials and mobilities in non-polar crystals, Phys. Rev. **80**, 72 (1950).

[53] P. J. Price, Two-dimensional electron transport in semiconductor layers. I. Phonon scattering, Ann. Phys. **133**, 217 (1981).

[54] J. Xi, M. Long, L. Tang, D. Wang, and Z. Shuai, First-principles prediction of charge mobility in carbon and organic nanomaterials, Nanoscale **4**, 4348 (2012).

[55] Y. Cai, G. Zhang, and Y. W. Zhang, Polarity-reversed robust carrier mobility in monolayer MoS_2 nanoribbons, J. Am. Chem. Soc. **136**, 6269 (2014).

[56] Y. Zhao, G. Gou, X. Lu, and Y. Hao, Intrinsic auxeticity and negative piezoelectricity in two-dimensional group-IV dipnictide monolayers with in-plane anisotropy, J. Mater. Chem. C **9**, 6068 (2021).

[57] J. Deb, N. Seriani, and U. Sarkar, Ultrahigh carrier mobility of penta-graphene: A first-principle study, Phys. E **127**, 114507 (2021).

[58] M. K. Li, S. J. Lee, and T. W. Kang, The mass effects on two-dimensional relativistic fermions, Curr. Appl. Phys. **9**, 769 (2009).

[59] T. G. Pedersen, Nonlinear optical response of relativistic energy bands: Application to phosphorene, Phys. Rev. B **95**, 235419 (2017).

[60] S. Das Sarma, S. Adam, E. H. Hwang, and E. Rossi, Electronic transport in two-dimensional graphene, Rev. Mod. Phys. **83**, 407 (2011).

[61] A. H. Castro Neto, F. Guinea, N. M. R. Peres, K. S. Novoselov, and A. K. Geim, The electronic properties of graphene, Rev. Mod. Phys. **81**, 109 (2009).

[62] M. Gajdoš, K. Hummer, G. Kresse, J. Furthmüller, and F. Bechstedt, Linear optical properties in the projector-augmented wave methodology, Phys. Rev. B **73**, 045112 (2006).